

CaCu₃Ru₄O₁₂: A High-Kondo-Temperature Transition-Metal Oxide

D. Takegami¹, C.-Y. Kuo,^{1,2} K. Kasebayashi,³ J.-G. Kim,⁴ C. F. Chang,¹ C. E. Liu,^{1,5} C. N. Wu,^{1,6} D. Kasinathan,¹ S. G. Altendorf,¹ K. Hofer,¹ F. Meneghin,¹ A. Marino,¹ Y. F. Liao,² K. D. Tsuei,² C. T. Chen,² K.-T. Ko,⁴ A. Günther,⁷ S. G. Ebbinghaus,⁸ J. W. Seo,¹ D. H. Lee,¹ G. Ryu,¹ A. C. Komarek,¹ S. Sugano,⁹ Y. Shimakawa,⁹ A. Tanaka,¹⁰ T. Mizokawa,¹¹ J. Kuneš,¹² L. H. Tjeng,^{1,*} and A. Hariki^{3,12,†}

¹Max Planck Institute for Chemical Physics of Solids, Nöthnitzer Straße 40, 01187 Dresden, Germany

²National Synchrotron Radiation Research Center, 101 Hsin-Ann Road, 30076 Hsinchu, Taiwan

³Department of Physics and Electronics, Osaka Prefecture University,

1-1 Gakuen-cho, Nakaku, Sakai, Osaka 599-8531, Japan

⁴Department of Physics, POSTECH, Pohang 37673, Korea

⁵Department of Electrophysics, National Yang Ming Chiao Tung University (NYCU),

Hsinchu 30010, Taiwan

⁶Department of Physics, National Tsing Hua University, Hsinchu 30013, Taiwan

⁷Experimental Physics V, University of Augsburg, 86135 Augsburg, Germany

⁸Institute of Chemistry, Martin Luther University Halle-Wittenberg, 06120 Halle, Germany

⁹Institute for Chemical Research, Kyoto University, Uji, Kyoto 611-0011, Japan

¹⁰Quantum Matter Program, Hiroshima University, Higashi-Hiroshima 739-8530, Japan

¹¹Department of Applied Physics, Waseda University, Shinjuku, Tokyo 169-8555, Japan

¹²Institute of Solid State Physics, TU Wien, 1040 Vienna, Austria

 (Received 28 May 2021; revised 10 November 2021; accepted 29 November 2021; published 26 January 2022)

We present a comprehensive study of CaCu₃Ru₄O₁₂ using bulk sensitive hard and soft x-ray spectroscopy combined with local-density approximation + dynamical mean-field theory (DMFT) calculations. Correlation effects on both the Cu and Ru ions can be observed. From the Cu 2*p* core-level spectra, we deduce the presence of magnetic Cu²⁺ ions hybridized with a reservoir of itinerant electrons. The strong photon energy dependence of the valence band allows us to disentangle the Ru, Cu, and O contributions and, thus, to optimize the DMFT calculations. The calculated spin and charge susceptibilities show that the transition metal oxide CaCu₃Ru₄O₁₂ must be classified as a Kondo system and that the Kondo temperature is in the range of 500–1000 K.

DOI: [10.1103/PhysRevX.12.011017](https://doi.org/10.1103/PhysRevX.12.011017)

Subject Areas: Condensed Matter Physics, Magnetism

Transition metal oxides show a wide variety of spectacular physical properties such as superconductivity, metal-insulator and spin-state transitions, unusually large magnetoresistance, orbital ordering phenomena, and multiferroicity [1–3]. Remarkably, heavy fermion or Kondo behavior is hardly encountered in oxides. While quite common in the rare-earth and actinide intermetallics [4–7], one may find perhaps only in the oxide LiV₂O₄ [8–10] indications for heavy fermion physics.

The discovery of the transition metal oxide CaCu₃Ru₄O₁₂ (CCRO) showing Kondo-like properties,

therefore, created quite an excitement [11–14]. The crystal structure of this A-site ordered perovskite is shown in the inset in Fig. 1. However, the Kondo interpretation has also met fierce reservations. It has been argued that the specific heat coefficient γ does not deviate much from the band structure value, suggesting a minor role of the electronic correlations [15]. Other interpretations of the mass enhancement have been put forward [16,17]. Electron spectroscopy studies have also not converged on the position or even the presence of the putative Kondo peak [18–20].

Here, we address the CCRO problem from a different perspective. Figure 1 shows the magnetic susceptibility of CCRO together with that of CaCu₃Ti₄O₁₂ (CCTO), as reproduced from Refs. [11,12,21,22] and Ref. [23], respectively. One can observe that CCTO follows, far above its 25 K Néel temperature, almost a textbook Curie-Weiss law that can be understood in terms of paramagnetic $S = 1/2$ Cu²⁺ ions. By contrast, one can also see that CCRO shows a completely different behavior with a magnetic

*hao.tjeng@cpfs.mpg.de

†hariki@pe.osakafu-u.ac.jp

Published by the American Physical Society under the terms of the [Creative Commons Attribution 4.0 International license](https://creativecommons.org/licenses/by/4.0/). Further distribution of this work must maintain attribution to the author(s) and the published article's title, journal citation, and DOI. Open access publication funded by the Max Planck Society.

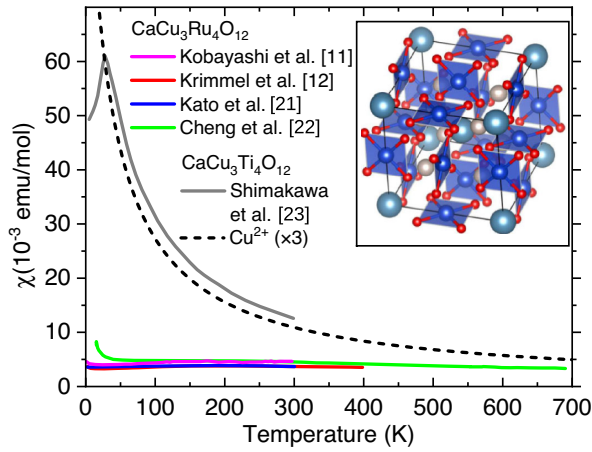


FIG. 1. Magnetic susceptibility of $\text{CaCu}_3\text{Ru}_4\text{O}_{12}$ reproduced from Refs. [11,12,21,22] and of $\text{CaCu}_3\text{Ti}_4\text{O}_{12}$ from Ref. [23]. The black dashed line shows the Curie paramagnetic behavior for a $S = 1/2$ Cu^{2+} ion scaled by a factor of 3. Inset: crystal structure of $\text{CaCu}_3\text{Ru}_4\text{O}_{12}$ visualized by VESTA [24]. The blue, red, gray, and indigo blue spheres represent Cu, O, Ru, and Ca atoms, respectively.

susceptibility that is an order of magnitude smaller. There are also no indications at all for magnetic order. If one believes that the system is nonmagnetic and that Kondo physics does not take place in CCRO, then the Cu ions in CCRO have to be monovalent with the nonmagnetic full-shell $3d^{10}$ configuration or trivalent, which can be a nonmagnetic band insulator like NaCuO_2 .

We show here that the Cu ions are definitely divalent and, thus, have a spin degree of freedom. We carry out a detailed photoelectron spectroscopy study using a wide range of photon energies in order to establish the presence of correlation effects on both the Cu and Ru ions as well as to disentangle the Ru, Cu, and O contributions to the valence band. This allows us to tune the double-counting corrections in the local-density approximation (LDA) + dynamical mean-field theory (DMFT) calculations accordingly, making these calculations predictive for low-energy physics. We then are able to determine how the Cu^{2+} magnetic moments can be screened. In particular, we show that, in going from high to low temperatures, this screening takes place already at 500–1000 K and that we, thus, must classify CCRO as a Kondo system with a very high Kondo temperature.

Hard x-ray photoemission (HAXPES) measurements are carried out at the Max-Planck-NSRRC HAXPES end station [25] at the Taiwan undulator beam line BL12XU of SPring-8 in Japan. The photon energy is set to $h\nu = 6.5$ keV, and the overall energy resolution is approximately 270 meV as determined from the Fermi cutoff of a gold reference sample. Soft x-ray (resonant) photoelectron (PES) and absorption (XAS) spectroscopy experiments are performed at the NSRRC-MPI TPS 45A submicron soft x-ray spectroscopy beam line at the Taiwan Photon Source

(TPS) in Taiwan. The overall energy resolution when using 1.2 keV, 931 eV, and 440 eV photons is approximately 150, 125, and 60 meV, respectively. Photoemission measurements in the vicinity of the Ru $4d$ Cooper minimum, i.e., at photon energies of 200, 150, and 100 eV, are performed at the PLS-II 4A1 micro-ARPES beam line of the Pohang Light Source (PLS) in Korea. The overall energy resolution is approximately 55 meV. Polycrystalline samples of CCRO are synthesized by solid-state reactions [26]. Clean sample surfaces are obtained by cleaving sintered samples *in situ* in ultrahigh vacuum preparation chambers with pressures in the low 10^{-10} mbar range. The measurements at SPring-8 and TPS are carried out at 80 K, and the measurements at PLS at 100 K. We use three different batches of CCRO samples for our spectroscopic measurements, all giving the same results, providing confidence in the reliability of the data; see the Appendix A.

Our calculations employ the LDA + DMFT scheme [27–29]. We start with density functional calculations for the experimental crystal structure [12] (see Fig. 1) using the Wien2k code [30] and construct the multiband Hubbard model on the basis spanned by the Cu $3d$, Ru $4d$, and O $2p$ Wannier functions obtained with the wannier90 package [31,32]. The on-site Coulomb interactions on the Cu and Ru sites are approximated with the density-density form with parameters $(U, J) = (8.5 \text{ eV}, 0.98 \text{ eV})$ for Cu $3d$ electrons and $(3.1 \text{ eV}, 0.7 \text{ eV})$ for Ru $4d$ electrons, which are typical values for Cu and Ru systems [19,33–35]. The continuous-time quantum Monte Carlo (CTQMC) method with the hybridization expansion [36–38] is used to solve the auxiliary Anderson impurity model (AIM). The double-counting corrections arising in LDA + X methods [29,39], which fix the charge-transfer energies on the Cu and Ru sites, are treated as adjustable parameters and their values fixed by comparison to the present valence band and core-level photoemission data as well as previous angle-resolved PES (ARPES) data. The valence spectra are obtained by analytic continuation of self-energy using the maximum entropy method [40,41]. The Cu $2p$ and Ru $3d$ core-level XPS are calculated using the method in Refs. [42–44].

We carry out XAS and valence band resonant PES measurements in the vicinity of the Cu $L_{2,3}$ edge; see Fig. 2. The peak positions and line shape of the spectra are characteristic for divalent Cu [19,45–47]. We can exclude that the Cu in CCRO is monovalent or trivalent, since the spectral features of Cu^{1+} and Cu^{3+} oxides are positioned at quite different energies [19,46,48]. We, thus, can conclude that the Cu ions in CCRO possess a spin degree of freedom and that some form of screening must take place to make their magnetic susceptibility deviate dramatically from the Curie-Weiss law.

Figure 3 shows the Cu $2p$ core-level HAXPES spectrum of CCRO together with that of Li_2CuO_2 as reproduced from Ref. [49]. Here, we take Li_2CuO_2 as a reference system which contains CuO_4 plaquettes that are weakly

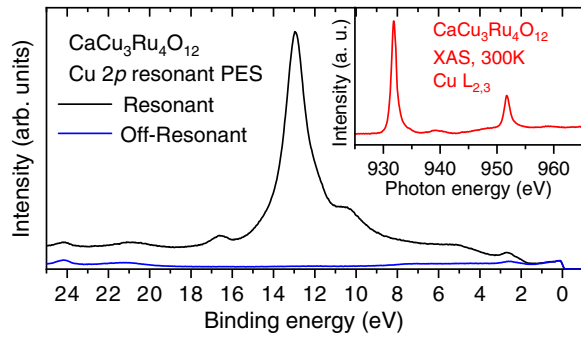


FIG. 2. Valence band resonant photoemission of CaCu₃Ru₄O₁₂, with the experimental spectra taken at the Cu 2*p* (*L*₃) resonance ($h\nu = 931.2$ eV) and at 10 eV below the resonance ($h\nu = 921.2$ eV). The inset displays the experimental Cu-*L*_{2,3} x-ray absorption spectrum.

coupled [49] and, thus, can serve for a comparison with CCRO, which also contains rather isolated CuO₄ plaquettes; see Fig. 1. The spectra share the gross features: the main peak (*B*) at around 932–933 eV binding energy and the satellite (*C*) at 942 eV for the Cu 2*p*_{3/2} component. However, the fine structure differs considerably: The main peak of CCRO consists of two peaks (*A* and *B*) [18,50] unlike the single peak (*B*) of Li₂CuO₂.

The Cu 2*p* core-level spectrum of Li₂CuO₂ is typical for a Cu²⁺ oxide [51]. Thanks to the weak coupling between the CuO₄ plaquettes, it can be explained accurately with a full multiplet single CuO₄-cluster calculation [52,53], as

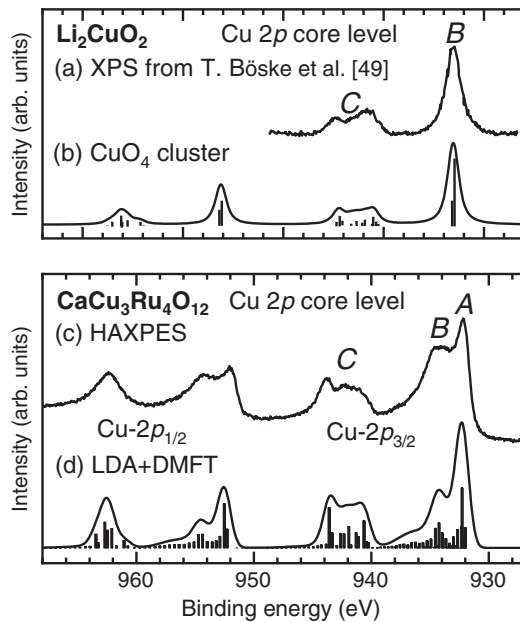


FIG. 3. (a) Experimental Cu 2*p* core-level x-ray photoemission spectrum of Li₂CuO₂ reproduced from Ref. [49]. (b) Theoretical spectrum from the CuO₄ cluster model. (c) Experimental Cu 2*p* core-level HAXPES spectrum of CaCu₃Ru₄O₁₂. (d) Theoretical spectrum from the LDA + DMFT method.

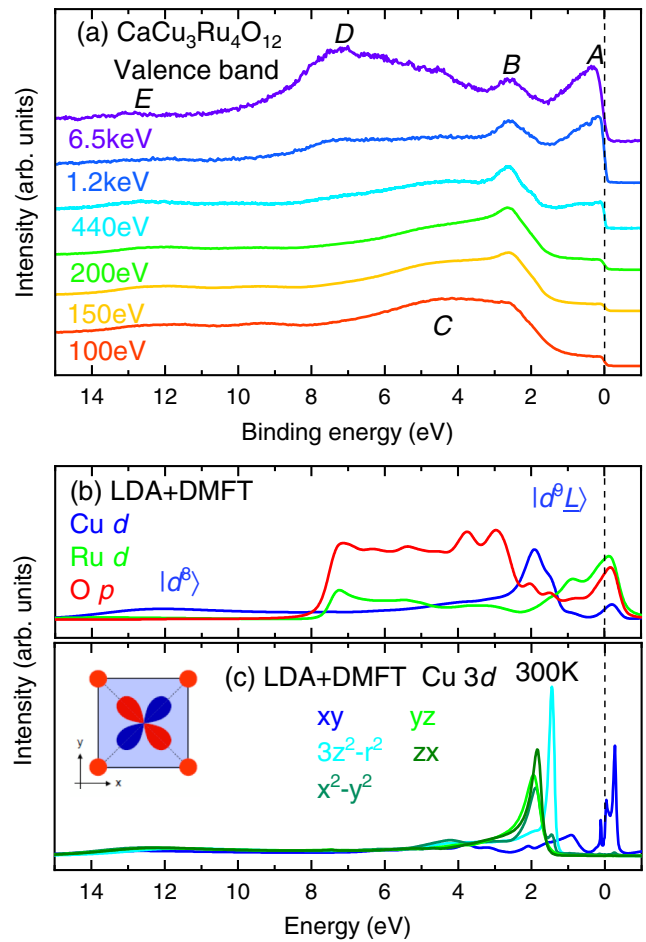


FIG. 4. Valence band spectra of CaCu₃Ru₄O₁₂: (a) experimental results measured at different photon energies and (b) LDA+DMFT spectral intensities for the Cu 3*d*, Ru 4*d*, and O 2*p* states. The spectral broadening is taken into account using a 200-meV Gaussian to simulate the experimental resolution. (c) LDA+DMFT spectral intensities of the Cu 3*d* orbitals in CaCu₃Ru₄O₁₂. The Cu orbitals are defined in the local axis of the CuO₄ plane, as shown in the inset.

shown in Fig. 3(b). In contrast, the two-peak structure (*A* and *B*) of the CCRO main peak cannot be captured by the cluster model. This is indicative of a screening process [18,50,54,55] which is present in CCRO but absent in Li₂CuO₂. Since the CuO₄ plaquettes in CCRO are quite isolated from each other, a nonlocal screening mechanism due to inter-Cu-cluster hopping is not expected to play an important role. We rather relate the screening process to the metallic state of CCRO. The LDA + DMFT calculations shown in Fig. 3(d) reproduce the fine structure of the main peak very well. We, thus, indeed can infer that CCRO contains correlated magnetic Cu²⁺ ions, which experience screening by conduction electrons. How strong or complete is the screening is discussed below.

Figure 4(a) shows the experimental valence band spectra of CCRO in a broad energy range measured at various photon energies. Our motivation here is to make use of the

different photon-energy dependence of the photoionization cross sections [56–58] to distinguish the Ru $4d$, Cu $3d$, and O $2p$ contributions to the spectra. The photon energy of 6.5 keV in HAXPES is much higher than the previously used photon energies of 1486.6 and 920 eV [18,19,50] and makes Ru $4d$ have the largest cross section relative to Cu $3d$ and O $2p$. The low photon energies of 200, 150, and 100 eV are close to the Cooper minimum of the Ru $4d$ cross section [58], so that with these photon energies the Ru $4d$ signal gets maximally suppressed, enabling us to observe better the Cu $3d$ contribution. The ratio between the O $2p$ and Cu $3d$ cross sections also becomes continuously larger with lowering the photon energy [58]. See also Appendix B displaying the photon energy dependence of the cross sections in more detail.

In the set of valence band spectra [Fig. 4(a)], we can identify features labeled *A*, *B*, *C*, *D*, and *E*. Features *A* and *D* are very strong at 6.5 keV and diminish almost completely between 100 and 200 eV. This strongly suggests that *A* and *D* are derived from the Ru $4d$ orbitals. Features *B* and *E* are visible throughout the set, while the intensity of *C* is enhanced at 100 eV, the lowest photon energy of the set. This observation indicates that features *B* and *E* are related to the Cu $3d$, while *C* is likely of O $2p$ origin. We point out that the positions of these five features do not change with the photon energy and coincide with the previously reported soft x-ray studies [18,19,50].

The LDA + DMFT results are presented in Fig. 4(b). They corroborate the above assignment. The calculated Ru $4d$ spectrum matches the experimental features *A* and *D*, while the theoretical Cu $3d$ spectrum explains well features *B* and *E*, the former being the Cu $|d^9 \underline{L}\rangle$ and the latter the Cu $|d^8\rangle$ final state [19,45–47]. Feature *C* is captured by the theoretical O $2p$ spectra. The calculations reveal that the spectrum around the Fermi level is dominated by hybridized Ru $4d$ and O $2p$ bands. In Fig. 4(c), the Cu $3d$ spectrum is decomposed into xy , $3z^2-r^2$, x^2-y^2 , yz , and zx components. As shown in the inset, the Cu $3d$ xy orbital points to the surrounding four oxygen sites. Therefore, the Cu $3d$ xy orbital hybridizes with the Ru $4d$ orbitals (via the O $2p$ orbitals) most strongly among the five Cu $3d$ orbitals. The Cu $3d$ xy spectral density near the Fermi level is quite low compared to the Ru $4d$ and O $2p$ one [see Fig. 4(b)], and most of its weight is above the Fermi level.

In order to experimentally detect the Cu contribution around the Fermi level, we focus on the larger peak at positive energies and the spectra taken at 150 eV, which is almost the photon energy to minimize the Ru $4d$ signal. The top in Fig. 5 displays a close-up of the spectra along with the corresponding gold reference spectrum taken under the same conditions. In order to look for the possible presence of states above the Fermi level, we divide the CCRO spectrum by the corresponding gold spectrum. The results are shown in the bottom in Fig. 5. We can identify clearly the presence of a sharp peak at about 0.07–0.08 eV above

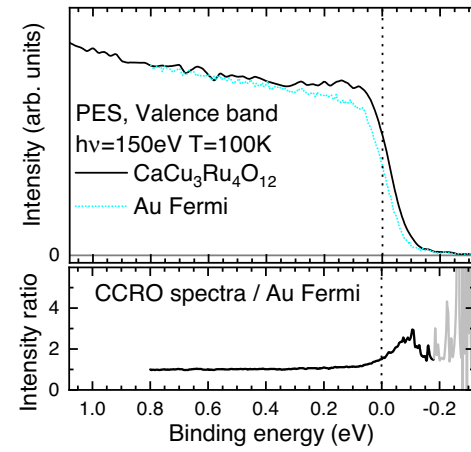


FIG. 5. Top: close-up of the Fermi-level region of the $\text{CaCu}_3\text{Ru}_4\text{O}_{12}$ spectrum together with the gold spectrum. Bottom: division of the $\text{CaCu}_3\text{Ru}_4\text{O}_{12}$ spectra by the gold spectrum.

the Fermi level, very consistent with the results of the LDA + DMFT calculations.

Enlarging to the vicinity of the Fermi level [59], the calculated Cu $3d$ xy spectrum in Fig. 6(a) reveals sharp temperature-dependent peaks. To put the present results in the context of Anderson impurity and periodic Anderson models, we show the Cu $3d$ xy hybridization densities in Fig. 6(b). The global view in the inset shows a strongly

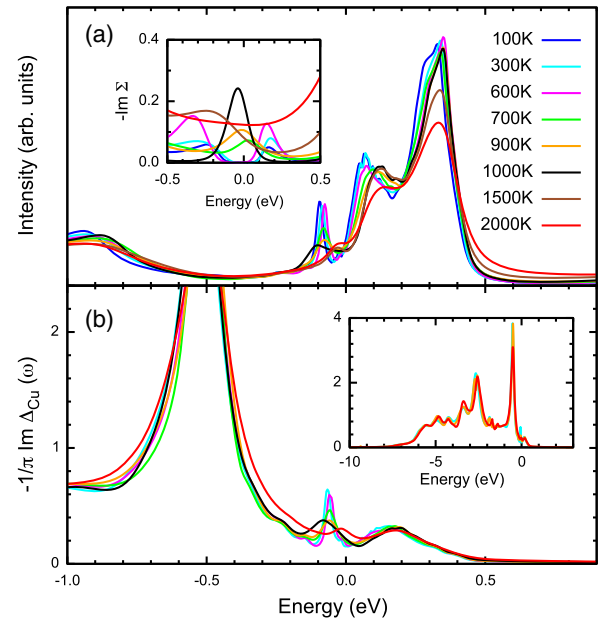


FIG. 6. (a) Temperature dependence of the Cu xy spectral intensities in the LDA + DMFT method. The inset shows the imaginary part of the self-energy of the Cu xy orbital. (b) LDA + DMFT hybridization densities $-1/\pi \text{Im}\Delta(\omega)$ of the Cu xy orbital. The inset shows the hybridization densities in a wide energy range for selected temperatures (300, 900, and 2000 K).

asymmetric situation with the Fermi energy located in the tail of the hybridization density. The hybridization density exhibits only a minor temperature dependence. A sharp hybridization peak below the Fermi level, responsible for the peak around -0.08 eV in the Cu spectra also observed with ARPES around the H point in the Brillouin zone [20], is an exception. This explains the different temperature behavior of the peaks in Fig. 6(a). Damping of the peaks above the Fermi level with increasing temperature is not accompanied by changes of the hybridization function and, thus, reflects the Anderson or Kondo impurity physics controlled by the Kondo temperature. Damping of the -0.08 eV peak arises from temperature-induced changes of the hybridization function, i.e., involves the feedback from the Cu ions (the temperature dependence of Ru contribution is negligible in the studied range). It is, therefore, an Anderson or Kondo lattice effect related to somewhat lower coherence temperature [60,61]. The inset in Fig. 6(a) shows the inverse quasiparticle lifetime. The region of long lifetime (dip in the inverse lifetime) between -0.1 and $+0.05$ eV around the Fermi level found at lower temperatures marks limits of the Fermi liquid theory. Between 600 and 700 K, the scattering rate around Fermi level increases, forming a peak in $\text{Im}\Sigma$. Eventually (1500–2000 K), the scattering rate grows quasiuniformly in the entire low-energy regime (-0.5 – 0.5 eV) with increasing temperature.

Next, we discuss the local spin susceptibility χ_{loc} at the Cu site. The top in Fig. 7 displays the χ_{loc} obtained with LDA + DMFT. It exhibits the Curie behavior at high temperatures and turns into a broad maximum at lower temperatures, which is characteristic for Kondo screening. The deviation from the Curie behavior starts around 1000 K, suggesting a relatively high Kondo scale T_K . The calculated χ_{loc} reproduces quite well the experimental susceptibility [11], although an exact match cannot be expected between the local and the uniform spin susceptibility, due to the contribution of the itinerant Ru $4d$ -O $2p$ states. The dynamical local susceptibility $\chi_{\text{loc}}(\omega)$ is, nevertheless, directly related to the spin-lattice relaxation rate

$1/T_1$ measured in nuclear magnetic resonance (NMR) experiments [12,21]:

$$\frac{1}{T_1} \propto T \lim_{\omega \rightarrow +0} \text{Im} \frac{\chi_{\text{loc}}(\omega)}{\omega}.$$

The calculated temperature dependence of $1/T_1$ is shown in Fig. 7. It shows an approximately linear increase at low temperatures, which flattens into a constant behavior at around 1000 K. It is well known that the former is characteristic of a Fermi liquid, while the latter of a fluctuating local moment. For CCRO, the NMR experiment is performed up to 700 K so far, where the absence of constant behavior is brought up as evidence against the Kondo physics in this compound. Our result, however, suggests that CCRO manifests its local moment signature in NMR above the reported temperature. The corresponding spin-spin correlation functions $\chi_{\text{spin}}(\tau)$ (see Appendix C) reflect the presence of an instantaneous Cu $3d$ moment at all temperatures, which rapidly disappears on a short timescale at temperatures below T_K . In contrast, the charge correlations are temperature independent. Rapid charge fluctuations present at all temperatures rather reflect the Cu—O bonding, not the hybridization with the states in the vicinity of the Fermi level.

The presence of magnetic Cu ions immersed in an itinerant band leads indeed to the emergence of Kondo physics, as demonstrated by our LDA + DMFT results. An important aspect for the long-standing discussions about CCRO is our finding that the Kondo temperature is quite high, namely, at around 700 K (between 500 and 1000 K). We note that the parameters and double-counting corrections in our LDA + DMFT calculations are tuned to reproduce the available experimental (HAX)PES and the recent ARPES [20] spectra; details can be found in Appendix D. In this respect, it is worth mentioning that we also include on-site Coulomb interactions at the Ru site. This is necessary to explain the presence of a satellite structure in the Ru $3d$ core-level PES spectrum; see Appendix D. It turns out that the inclusion of U_{Ru} in the Ru $4d$ shell has also a substantial influence on the low-energy properties of CCRO. We calculate the local spin susceptibility χ_{loc} at the Cu site with $U_{\text{Ru}} = 3.1$ eV and $U_{\text{Ru}} = 0.0$ eV (see Appendix D), indicating that correlations on the Ru site influence the screening process on the Cu site. This can be traced back to the influence of the Ru U on the shape of the Ru $4d$ -O $2p$ band. In Appendix D, we show the Cu xy spectral intensities calculated with $U_{\text{Ru}} = 0$ eV on the Ru $4d$ shell, where the agreement to the available PES data is surrendered.

The high Kondo temperature we find from our LDA + DMFT calculations implies that the contribution of the Kondo screening process to the low-temperature specific heat is modest, thus explaining why band structure calculations can seemingly reproduce the experimentally

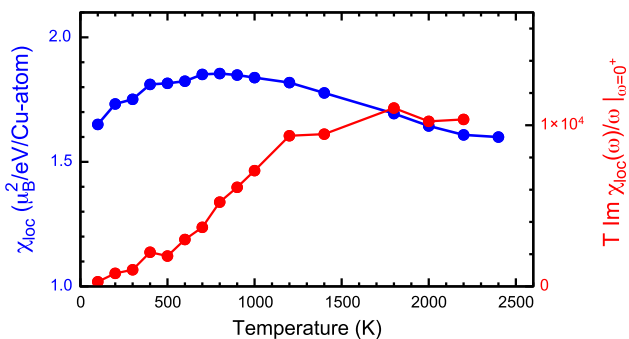


FIG. 7. Local susceptibility $\chi_{\text{loc}}(T)$ (blue) and the dynamical spin susceptibility $\chi_{\text{loc}}(\omega = +0)$ (red), calculated by the LDA + DMFT method.

observed γ value of the specific heat rather well, since the main contribution comes from the uncorrelated Ru-O-derived bands. The high Kondo temperature also implies that one needs to go to very high temperatures to see the appearance of local Cu moments, as demonstrated in Fig. 7. We can, thus, infer that upon going from high to low temperatures the Kondo screening process is practically completed already at 300 K and that lowering the temperature further does not produce significant changes in the electronic and magnetic properties. It is understandable that there has been a controversy concerning Kondo physics in $\text{CaCu}_3\text{Ru}_4\text{O}_{12}$, since its signatures in low-temperature measurements are weak.

Nevertheless, Kondo physics is present, as evidenced by the low-temperature disappearance of the Cu^{2+} magnetic susceptibility for which we are able to provide a quantitative explanation using our LDA + DMFT calculations that include fine-tuning of the parameters from a detailed comparison to bulk-sensitive photoemission data. Our findings indicate that the material class $\text{CaCu}_3\text{M}_4\text{O}_{12}$ indeed provides a unique opportunity to explore Kondo phenomena in transition metal compounds, where one may achieve lower Kondo temperatures by suitably varying the M constituent.

ACKNOWLEDGMENTS

The authors thank Sebastian Huber for discussions and benchmark NRG calculations, and Andrii Sotnikov for discussions in the early stage of this work. A. H. and J. K. are supported by the European Research Council (ERC) under the European Union's Horizon 2020 research and innovation program (Grant Agreement No. 646807-EXMAG). A. H. was supported by JSPS KAKENHI Grant No. 21K13884. The computations were performed at the Vienna Scientific Cluster (VSC). The research in Dresden is supported by the Deutsche Forschungsgemeinschaft (DFG) through Grant No. 320571839 and SFB 1143 (Project-ID No. 247310070). The experiments in Taiwan and Korea were facilitated by the Max Planck-POSTECH-Hsinchu Center for Complex Phase Materials. K. K. and K.-T. K. were supported by National Research Foundation of Korea (NRF) through the Max Planck-POSTECH Initiative (No. 2016K1A4A4A01922028). S. S. and Y. S. are supported by JSPS KAKENHI Grants-in-Aid for Scientific Research (No. 19H05823 and No. 20H00397) and by a JSPS Core-to-Core Program (A) Advanced Research Networks.

APPENDIX A: SAMPLE CONSISTENCY

In order to ensure that the experimental spectra and their features are intrinsic to the material, we utilize three different batches of samples synthesized by three different groups: A.C. Komarek's group from Max Planck Institute for Chemical Physics of Solids, Dresden, A. Günther from

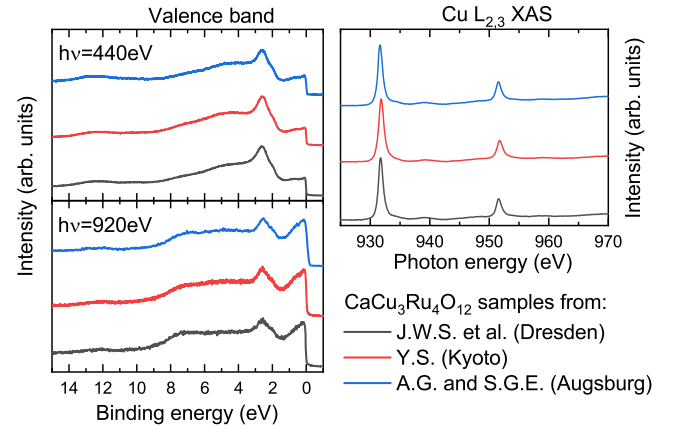


FIG. 8. Valence band PES (left) and Cu- $L_{2,3}$ XAS (right) of $\text{CaCu}_3\text{Ru}_4\text{O}_{12}$ samples synthesized by the different groups used in this work.

the University of Augsburg, and Y. Shimakawa's group from the Kyoto University. Figure 8 shows the comparison of the valence band PES and XAS spectra taken from these three batches of samples.

The results match perfectly and, thus, confirm that the data presented in this paper are not sample specific nor due to extrinsic contributions.

APPENDIX B: PHOTOIONIZATION CROSS SECTIONS

For the valence band of $\text{CaCu}_3\text{Ru}_4\text{O}_{12}$, the most relevant contributions are Cu $3d$, Ru $4d$, and O $2p$. Figure 9 shows the photon energy dependence of the photoionization cross sections as interpolated from the data tabulated in Refs. [56–58]. The vertical lines highlight the photon energies used in this study. At high photon energies (HAXPES, 6.5 keV), the Ru $4d$ provides a larger signal

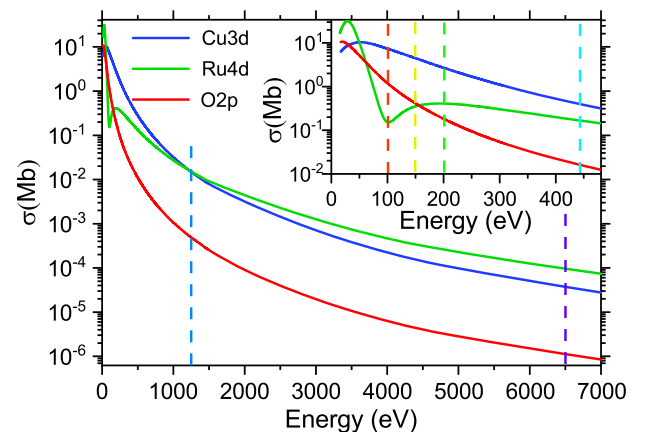


FIG. 9. Photoionization cross section values of Cu $3d$, Ru $4d$, and O $2p$ interpolated from the data tabulated in Refs. [56–58]. The vertical lines indicate the photon energies used for the photoemission data shown in Fig. 4.

than the Cu 3*d* and the O 2*p*. Going to lower photon energies, the Cu 3*d* becomes gradually stronger, and, with a crossover at 1.2 keV, it becomes the dominant contributor. At around 100 eV, there is a minimum in the Ru 4*d* cross section, also known as the Cooper minimum, which provides the ideal condition for studying the Cu 3*d* contributions. At this photon energy, the Cu 3*d* signal is enhanced by a factor of approximately 70 with respect to the Ru 4*d*. For lower photon energies, the Ru 4*d* quickly gains strength and becomes again the dominant contributor, making these low photon energies less useful when searching for the Cu 3*d* signal close to the Fermi level. As for the O 2*p* contribution, we observe that it is highly suppressed for high energies but becomes competitive with the Cu 3*d* only for energies below approximately 50 eV.

APPENDIX C: LDA + DMFT COMPUTATIONAL METHOD

Below, we describe the LDA + DMFT scheme [27–29] employed to analyze the experimental data. We start with density functional calculations for the experimental crystal structure of CCRO [12] using the Wien2k code [30]. Then, we construct the multiband Hubbard model on the basis spanned by the Cu 3*d*, Ru 4*d*, and O 2*p* Wannier functions from the LDA bands using wien2wannier and wannier90 packages [31,32]. The multiband Hubbard model is augmented with the local electron-electron interaction within the Cu 3*d* and Ru 4*d* shells giving the Hamiltonian

$$H = \sum_{\mathbf{k}} \begin{pmatrix} \mathbf{c}_{\mathbf{k}}^{\dagger} & \mathbf{r}_{\mathbf{k}}^{\dagger} & \mathbf{p}_{\mathbf{k}}^{\dagger} \end{pmatrix} \begin{pmatrix} h_{\mathbf{k}}^{cc} - \mu_{\text{cr}}^{\text{Ru}} & h_{\mathbf{k}}^{dp} & h_{\mathbf{k}}^{cp} \\ h_{\mathbf{k}}^{rc} & h_{\mathbf{k}}^{rr} - \mu_{\text{dc}}^{\text{Cu}} & h_{\mathbf{k}}^{rp} \\ h_{\mathbf{k}}^{pc} & h_{\mathbf{k}}^{pr} & h_{\mathbf{k}}^{pp} \end{pmatrix} \begin{pmatrix} \mathbf{c}_{\mathbf{k}} \\ \mathbf{r}_{\mathbf{k}} \\ \mathbf{p}_{\mathbf{k}} \end{pmatrix} + \sum_i W_{i,\text{Cu}}^{dd} + \sum_i W_{i,\text{Ru}}^{dd}.$$

Here, $\mathbf{c}_{\mathbf{k}}^{\dagger}$ is an operator-valued vector whose elements are Fourier transforms of $c_{\gamma i}$ that annihilate the Cu 3*d* electron in the orbital γ in the i th unit cell. Similarly, $\mathbf{r}_{\mathbf{k}}^{\dagger}$ and $\mathbf{p}_{\mathbf{k}}^{\dagger}$ are those for Ru 4*d* and O 2*p* electrons, respectively. The on-site Coulomb interaction $W_{i,\text{Cu}}^{dd}$ and $W_{i,\text{Ru}}^{dd}$ on Cu and Ru sites is approximated with the density-density form with parameters $(U, J) = (8.5 \text{ eV}, 0.98 \text{ eV})$ for Cu 3*d* electrons and $(3.1 \text{ eV}, 0.7 \text{ eV})$ for Ru 4*d* electrons, which are typical values for Cu and Ru systems [19,33–35]. The double-counting terms $\mu_{\text{dc}}^{\text{Ru}}$ and $\mu_{\text{dc}}^{\text{Cu}}$, which correct for the *d-d* interaction present in the LDA step [29,39], renormalize the *p-d* splitting and, thus, the charge-transfer energy. We fix the double-counting values to $\mu_{\text{dc}}^{\text{Cu}} = 70.1 \text{ eV}$ and $\mu_{\text{dc}}^{\text{Ru}} = 16.2 \text{ eV}$ ($\mu_{\text{dc}}^{\text{Ru}} = 13.4 \text{ eV}$ for the model without Ru e_g states) by comparison to the photoemission spectroscopy data discussed in Appendix D. The CTQMC method with the hybridization expansion [36–38,62] is used to solve the auxiliary AIM in the DMFT self-consistent calculation.

The valence spectra are obtained by analytic continuation of self-energy $\Sigma(\epsilon)$ using the maximum entropy method [40,41]. The hybridization function $\Delta(\epsilon)$ for the Cu 3*d* orbital γ ($|d_{\gamma}\rangle$) is given by [28,29]

$$\Delta_{\gamma}(\epsilon) = \langle d_{\gamma} | \epsilon - h_0 - \Sigma(\epsilon) - G^{-1}(\epsilon) | d_{\gamma} \rangle,$$

where $G(\epsilon)$ and h_0 are the local Green's function and the one-body part of the on-site Hamiltonian at the Cu site, respectively. $\Delta(\epsilon)$ does not depend on the spin, and small off-diagonal elements between different orbitals are neglected. The Cu 2*p* core-level spectrum is calculated using the method in Refs. [42,43], where the AIM with the DMFT hybridization density is extended to include the Cu 2*p* core orbitals [42,44]. The configuration interaction scheme with 25 bath states representing the DMFT hybridization density is employed to evaluate the 2*p* spectra.

Figure 10 shows the local spin $\chi_{\text{spin}}(\tau)$ and charge $\chi_{\text{charge}}(\tau)$ correlation functions at the Cu site. $\chi_{\text{spin}}(\tau)$ is given as $\chi_{\text{spin}}(\tau) = \langle \hat{m}_z(\tau) \hat{m}_z(0) \rangle$ [63,64], and $\chi_{\text{charge}}(\tau)$ is given by $\chi_{\text{charge}}(\tau) = \langle \delta \hat{n}(\tau) \delta \hat{n}(0) \rangle$ [65], where $\delta \hat{n} = \hat{n} - \langle \hat{n} \rangle$ with the Cu *d*-occupation number operator \hat{n} . These quantities are calculated by the impurity Anderson model with the DMFT hybridization using the CTQMC method. The local susceptibility $\chi_{\text{loc}}(T)$ is obtained by integrating the $\chi_{\text{spin}}(\tau)$ at temperature T with respect to the imaginary time τ :

$$\chi_{\text{loc}}(T) = \int_0^{1/T} d\tau \langle m_z(\tau) m_z(0) \rangle.$$

A rigid instantaneous Cu 3*d* spin moment is present for all temperatures, as imprinted in the temperature-independent value of $\chi_{\text{spin}}(\tau = 0)$; see Fig. 10. The spin moment survives on a long timescale at high temperatures (see,

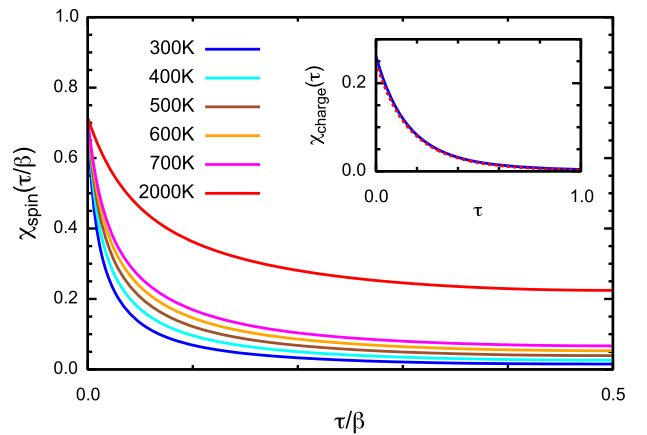


FIG. 10. Correlation function $\chi(\tau)$ of the spin and charge (inset) channel calculated by the LDA + DMFT method, where $\beta = 1/k_B T$ is the inverse temperature.

e.g., at 2000 K), giving the Curie behavior in χ_{loc} shown in the main text, while it disappears on short timescales at low temperatures due to the Kondo screening by the Ru $4d$ -O $2p$ bands, giving the Pauli-like behavior in χ_{loc} . In contrast to the temperature dependence in $\chi_{\text{spin}}(\tau/\beta)$, the local charge correlation function χ_{charge} is substantially suppressed at all temperatures (see the inset in Fig. 10), indicating the frozen charge fluctuation of the Cu $3d$ electrons in CCRO, as expected in the Kondo regime. Thus, the calculated spin and charge correlation functions support the Kondo behavior of Cu $3d$ electrons in the studied material. We point out that the $\chi_{\text{spin}}(\tau = 0)$ value is reduced to 0.7 from 1.0, which corresponds to the $S = 1/2$ Kondo limit. The reduction comes from the mixture of the $|d^{10}\underline{L}\rangle$ configuration by the Cu-O hybridization, where $|\underline{L}\rangle$ represents an O $2p$ hole, but it does not show a temperature dependence. This behavior characterizes the effect of charge transfer in the Cu-O subsystem. The energy scale of the Kondo physics, therefore, builds on the ligand-metal hybridization in addition to the Coulomb interaction U at the Cu site.

APPENDIX D: PARAMETERS IN THE LDA + DMFT SIMULATION

In the calculations, we use two versions of the model described in Appendix C. The first model contains all Ru $4d$ states, while the second contains only the Ru t_{2g} states present at and below the Fermi level. The first model, which we consider as the primary one, is needed to capture the full spectrum, in particular, feature *D* in Fig. 4(a). The second model is used for numerical convenience, as it allows us to perform LDA + DMFT calculations at a lower temperature (below 300 K). It is employed to compute the low-energy Cu spectral intensities (Fig. 6) and response functions (Fig. 7) including temperatures below 300 K. Its results are validated by comparison to the first model at the higher temperatures.

The parameters $\mu_{\text{dc}}^{\text{Cu}}$ and $\mu_{\text{dc}}^{\text{Ru}}$ of our theory (Appendix C) are fixed to reproduce (i) positions of peaks *A–E* in the valence photoemission spectra in Fig. 4, (ii) positions of the low-energy peak at 0.07–0.08 eV above (Fig. 5) and around 0.08 eV below [20] the Fermi energy, (iii) the splitting of the Cu $2p_{3/2}$ XPS main line (see Fig. 3), and (iv) observation of a shoulder in the Ru $3d$ core-level XPS spectrum (see Fig. 12).

Before analyzing $\mu_{\text{dc}}^{\text{Cu}}$ and $\mu_{\text{dc}}^{\text{Ru}}$, we briefly discuss why we need to include the electron-electron interaction on the Ru site [66–68]. To this end, we compare calculations with $U_{\text{Ru}} = 3.1$ eV from previous DFT studies for Ru oxides (with the same formal Ru valence as in CCRO) [34,35] and with $U_{\text{Ru}} = 0.0$ eV. Figure 12(a) shows that finite U_{Ru} is needed to yield the shoulder or satellite feature (iv) in the Ru $3d$ core-level XPS spectra. However, finite U_{Ru} affects also the behavior of the Cu xy state [see dashed lines in

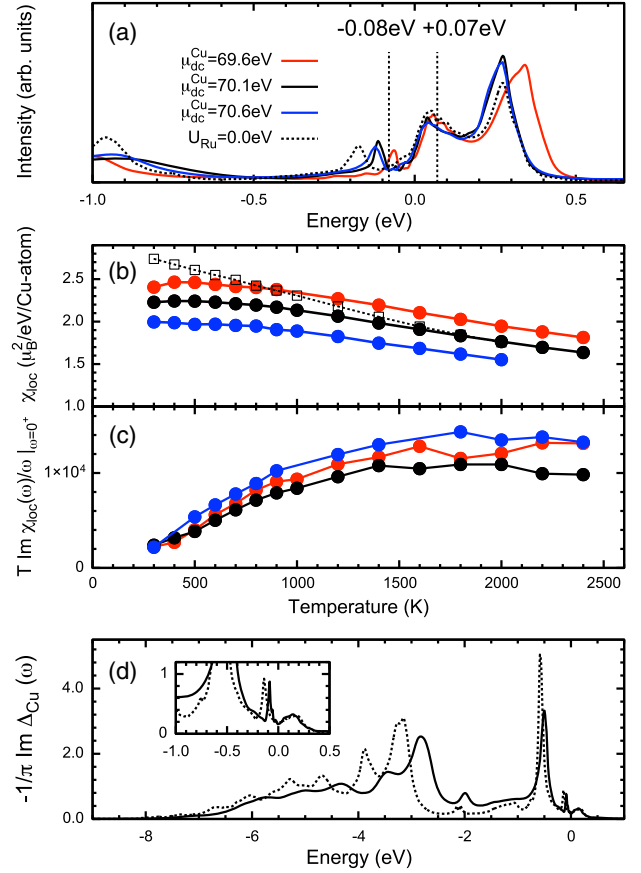


FIG. 11. (a) The Cu xy spectral intensities in LDA + DMFT results for different double-counting $\mu_{\text{dc}}^{\text{Cu}}$ values. The positions of the low-energy peak in the experimental PES data are indicated by vertical dashed lines. The calculation is performed at 300 K. (b) Local susceptibility $\chi_{\text{loc}}(T)$ and (c) dynamical spin susceptibility $\chi_{\text{loc}}(\omega = +0)$ at the Cu site. Here, the model with all Ru $4d$ states is employed. The dashed lines in (a) and (b) show the results obtained with $U_{\text{Ru}} = 0.0$ eV. (d) Hybridization densities $-1/\pi \text{Im} \Delta(\omega)$ of the Cu xy orbital in LDA + DMFT with $U_{\text{Ru}} = 3.1$ eV (solid line) and with $U_{\text{Ru}} = 0.0$ eV (dashed line). The inset shows the hybridization densities near E_F .

Figs. 11(a) and 11(b)], through dynamical renormalization (band narrowing) of Ru bands, which modifies the environment (hybridization density) of Cu; see Fig. 11(d). With $U_{\text{Ru}} = 0.0$ eV, we cannot find $\mu_{\text{dc}}^{\text{Cu}}$ to fulfill (i)–(iii). We note that the Ru spin response is far from the Curie form despite the presence of correlations in the Ru $4d$ shell; see Fig. 12(b). Correspondingly, also the screened (effective) Ru moment is substantially smaller than the atomic value (approximately $2\mu_B$) for a Ru^{4+} ion.

The value of $\mu_{\text{dc}}^{\text{Cu}}$ affects the positions of the Cu d^8 satellite, feature *E*, and feature *B* in Fig. 4 as well as the low-energy peaks (ii). All of these are well reproduced by its chosen value of $\mu_{\text{dc}}^{\text{Cu}} = 70.1$ eV; see Figs. 11(a) and 4. The small screened spin susceptibility due to the Kondo screening is found around the optimal $\mu_{\text{dc}}^{\text{Cu}}$ value; see Figs. 11(b) and 11(c).

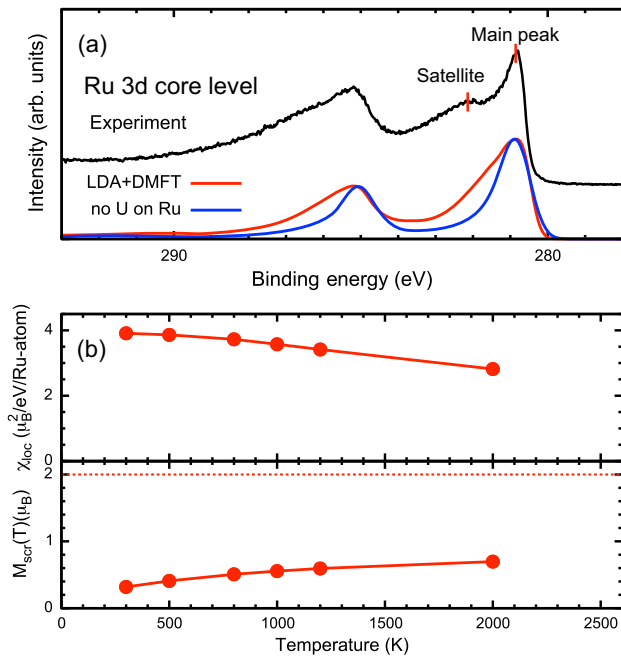


FIG. 12. (a) Experimental Ru 3d core-level photoemission spectrum of CaCu₃Ru₄O₁₂ (black line) and theoretical spectra from the LDA + DMFT calculation with $U_{\text{Ru}} = 3.1$ eV (red line) and $U_{\text{Ru}} = 0.0$ eV (blue line). (b) Top: local spin susceptibility and bottom: screened spin moment $M_{\text{scr}}(T) = \sqrt{T\chi_{\text{loc}}(T)}$ [63,64] on the Ru site computed by the LDA + DMFT method. The horizontal dashed line indicates the atomic value of the Ru⁴⁺ ion.

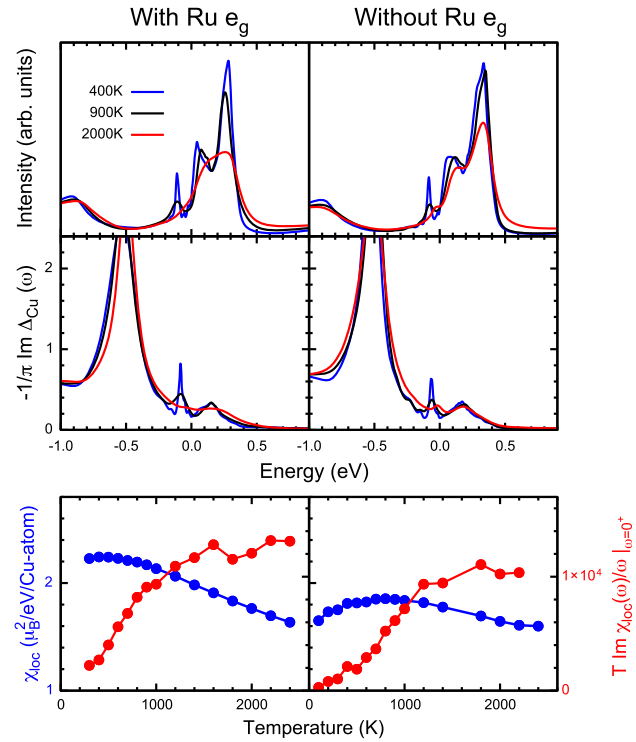


FIG. 14. LDA + DMFT results for the models (left) with and (right) without the Ru 4d e_g states at selected temperatures. Top: Cu xy spectral intensities; middle: the hybridization densities of the Cu xy orbitals; bottom: local susceptibility $\chi_{\text{loc}}(T)$ and the dynamical spin susceptibility $\chi_{\text{loc}}(\omega = +0)$ at the Cu site. $\mu_{\text{dc}}^{\text{Cu}} = 70.1$ eV is employed in the two models, and $\mu_{\text{dc}}^{\text{Ru}} = 16.2$ eV ($\mu_{\text{dc}}^{\text{Ru}} = 13.4$ eV) for the model with (without) Ru 4d e_g states.

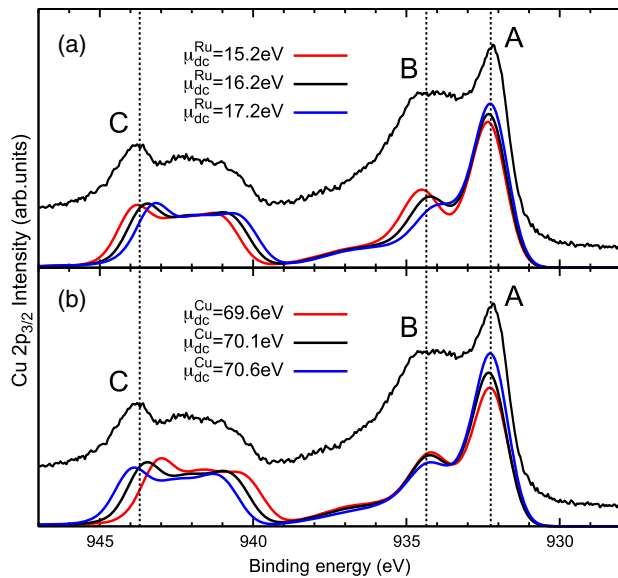


FIG. 13. (a) Cu $2p_{3/2}$ core-level photoemission spectra calculated by the LDA + DMFT method with selected $\mu_{\text{dc}}^{\text{Ru}}$ values (with $\mu_{\text{dc}}^{\text{Cu}} = 70.1$ eV). (b) The spectra by LDA + DMFT with selected $\mu_{\text{dc}}^{\text{Cu}}$ values (with $\mu_{\text{dc}}^{\text{Ru}} = 16.2$ eV). The experimental spectrum is shown for comparison.

The $\mu_{\text{dc}}^{\text{Cu}}$ also affects the Cu-O charge-transfer energy and, thus, the splitting between the main line and charge-transfer satellite in Cu $2p$ XPS; see Fig. 13(b). On the other hand, the behavior of Cu, including variation of $\mu_{\text{dc}}^{\text{Cu}}$, has a minor effect on its hybridization function, except for the peak just below the Fermi energy. As a result, the splitting of Cu $2p$ XPS main line (A, B) is independent of $\mu_{\text{dc}}^{\text{Cu}}$; see Fig. 13(b).

The same is not true for $\mu_{\text{dc}}^{\text{Ru}}$. Affecting primarily the Ru-O charge-transfer energy, its variation modifies the Cu $3d$ xy hybridization function around the Fermi level, which has a sizable effect on the splitting in the Cu $2p$ XPS main line (A, B); see Fig. 13(a). We can, thus, use (iii) together with the Ru features in the global spectrum (i) to establish $\mu_{\text{dc}}^{\text{Ru}} = 16.2$ eV.

Finally, we discuss the relationship of models with and without Ru 4d e_g states. While $\mu_{\text{dc}}^{\text{Cu}}$ is the same for the two models, $\mu_{\text{dc}}^{\text{Ru}}$ must be different, since the models include interaction between all Ru 4d orbitals in one case and between the t_{2g} only in the other one. The matching $\mu_{\text{dc}}^{\text{Ru}}$ for the model without Ru 4d e_g states is 13.2 eV. Both models yield very similar temperature dependencies of the Cu spectral functions as well as hybridization densities and local susceptibilities, as shown in Fig. 14.

- [1] R. J. Cava, *Oxide Superconductors*, *J. Am. Ceram. Soc.* **83**, 5 (2000).
- [2] D. Khomskii, *Transition Metal Compounds* (Cambridge University Press, Cambridge, England, 2014).
- [3] B. Keimer, S. A. Kivelson, M. R. Norman, S. Uchida, and J. Zaanen, *From Quantum Matter to High-Temperature Superconductivity in Copper Oxides*, *Nature (London)* **518**, 179 (2015).
- [4] G. R. Stewart, *Heavy-Fermion Systems*, *Rev. Mod. Phys.* **56**, 755 (1984).
- [5] P. Coleman, *Heavy Fermions: Electrons at the Edge of Magnetism*, arXiv:cond-mat/0612006.
- [6] C. Pfleiderer, *Superconducting Phases of f-Electron Compounds*, *Rev. Mod. Phys.* **81**, 1551 (2009).
- [7] S. Wirth and F. Steglich, *Exploring Heavy Fermions from Macroscopic to Microscopic Length Scales*, *Nat. Rev. Mater.* **1**, 16051 (2016).
- [8] S. Kondo, D. C. Johnston, C. A. Swenson, F. Borsa, A. V. Mahajan, L. L. Miller, T. Gu, A. I. Goldman, M. B. Maple, D. A. Gajewski, E. J. Freeman, N. R. Dilley, R. P. Dickey, J. Merrin, K. Kojima, G. M. Luke, Y. J. Uemura, O. Chmaissem, and J. D. Jorgensen, *LiV₂O₄: A Heavy Fermion Transition Metal Oxide*, *Phys. Rev. Lett.* **78**, 3729 (1997).
- [9] C. Urano, M. Nohara, S. Kondo, F. Sakai, H. Takagi, T. Shiraki, and T. Okubo, *LiV₂O₄ Spinel as a Heavy-Mass Fermi Liquid: Anomalous Transport and Role of Geometrical Frustration*, *Phys. Rev. Lett.* **85**, 1052 (2000).
- [10] A. Shimoyamada, S. Tsuda, K. Ishizaka, T. Kiss, T. Shimojima, T. Togashi, S. Watanabe, C. Q. Zhang, C. T. Chen, Y. Matsushita, H. Ueda, Y. Ueda, and S. Shin, *Heavy-Fermion-like State in a Transition Metal Oxide LiV₂O₄ Single Crystal: Indication of Kondo Resonance in the Photoemission Spectrum*, *Phys. Rev. Lett.* **96**, 026403 (2006).
- [11] W. Kobayashi, I. Terasaki, J.-i. Takeya, I. Tsukada, and Y. Ando, *A Novel Heavy-Fermion State in CaCu₃Ru₄O₁₂*, *J. Phys. Soc. Jpn.* **73**, 2373 (2004).
- [12] A. Krimmel, A. Günther, W. Kraetschmer, H. Dekinger, N. Büttgen, A. Loidl, S. G. Ebbinghaus, E.-W. Scheidt, and W. Scherer, *Non-Fermi-Liquid Behavior in CaCu₃Ru₄O₁₂*, *Phys. Rev. B* **78**, 165126 (2008).
- [13] A. Krimmel, A. Günther, W. Kraetschmer, H. Dekinger, N. Büttgen, V. Eyert, A. Loidl, D. V. Sheptyakov, E.-W. Scheidt, and W. Scherer, *Intermediate-Valence Behavior of the Transition-Metal Oxide CaCu₃Ru₄O₁₂*, *Phys. Rev. B* **80**, 121101(R) (2009).
- [14] T.-H. Kao, H. Sakurai, S. Yu, H. Kato, N. Tsujii, and H.-D. Yang, *Origin of the Magnetic Susceptibility Maximum in CaCu₃Ru₄O₁₂ and Electronic States in the A-Site Substituted Compounds*, *Phys. Rev. B* **96**, 024402 (2017).
- [15] H. Xiang, X. Liu, E. Zhao, J. Meng, and Z. Wu, *First-Principles Study on the Conducting Mechanism of the Heavy-Fermion System CaCu₃Ru₄O₁₂*, *Phys. Rev. B* **76**, 155103 (2007).
- [16] S. Tanaka, N. Shimazui, H. Takatsu, S. Yonezawa, and Y. Maeno, *Heavy-Mass Behavior of Ordered Perovskites ACu₃Ru₄O₁₂ (A = Na, Ca, La)*, *J. Phys. Soc. Jpn.* **78**, 024706 (2009).
- [17] S. Tanaka, H. Takatsu, S. Yonezawa, and Y. Maeno, *Suppression of the Mass Enhancement in CaCu₃Ru₄O₁₂*, *Phys. Rev. B* **80**, 035113 (2009).
- [18] T. Sudayama, Y. Wakisaka, K. Takubo, T. Mizokawa, W. Kobayashi, I. Terasaki, S. Tanaka, Y. Maeno, M. Arita, H. Namatame, and M. Taniguchi, *Bulk-Sensitive Photoemission Study of ACu₃Ru₄O₁₂ (A = Ca, Na, and La) with Heavy-Fermion Behavior*, *Phys. Rev. B* **80**, 075113 (2009).
- [19] N. Hollmann, Z. Hu, A. Maignan, A. Günther, L.-Y. Jang, A. Tanaka, H.-J. Lin, C. T. Chen, P. Thalmeier, and L. H. Tjeng, *Correlation Effects in CaCu₃Ru₄O₁₂*, *Phys. Rev. B* **87**, 155122 (2013).
- [20] H. Liu, Y. Cao, Y. Xu, D. J. Gawryluk, E. Pomjakushina, S.-Y. Gao, P. Dudin, M. Shi, L. Yan, Y.-F. Yang, and H. Ding, *Observation of Flat Bands due to Band Hybridization in the 3d-Electron Heavy-Fermion Compound CaCu₃Ru₄O₁₂*, *Phys. Rev. B* **102**, 035111 (2020).
- [21] H. Kato, T. Tsuruta, M. Matsumura, T. Nishioka, H. Sakai, Y. Tokunaga, S. Kambe, and R. E. Walstedt, *Temperature-Induced Change in the Magnitude of the Effective Density of States: A NQR/NMR Study of the A-Site-Ordered Perovskite System CaCu₃Ru₄O₁₂*, *J. Phys. Soc. Jpn.* **78**, 054707 (2009).
- [22] J.-G. Cheng, J.-S. Zhou, Y.-F. Yang, H. D. Zhou, K. Matsubayashi, Y. Uwatoko, A. MacDonald, and J. B. Goodenough, *Possible Kondo Physics near a Metal-Insulator Crossover in the A-Site Ordered Perovskite CaCu₃Ir₄O₁₂*, *Phys. Rev. Lett.* **111**, 176403 (2013).
- [23] Y. Shimakawa, *A-Site-Ordered Perovskites with Intriguing Physical Properties*, *Inorg. Chem.* **47**, 8562 (2008).
- [24] K. Momma and F. Izumi, *VESTA3 for Three-Dimensional Visualization of Crystal, Volumetric and Morphology Data*, *J. Appl. Crystallogr.* **44**, 1272 (2011).
- [25] J. Weinen, T. C. Koethe, C. F. Chang, S. Agrestini, D. Kasinathan, Y. F. Liao, H. Fujiwara, C. Schler-Langeheine, F. Strigari, T. Haupricht, G. Panaccione, F. Offi, G. Monaco, S. Huotari, K.-D. Tsuei, and L. H. Tjeng, *Polarization Dependent Hard X-Ray Photoemission Experiments for Solids: Efficiency and Limits for Unraveling the Orbital Character of the Valence Band*, *J. Electron Spectrosc. Relat. Phenom.* **198**, 6 (2015).
- [26] S. G. Ebbinghaus, A. Weidenkaff, and R. J. Cava, *Structural Investigations of ACu₃Ru₄O₁₂ (A = Na, Ca, Sr, La, Nd)—A Comparison between XRD-Rietveld and EXAFS Results*, *J. Solid State Chem.* **167**, 126 (2002).
- [27] W. Metzner and D. Vollhardt, *Correlated Lattice Fermions in d = ∞ Dimensions*, *Phys. Rev. Lett.* **62**, 324 (1989).
- [28] A. Georges, G. Kotliar, W. Krauth, and M. J. Rozenberg, *Dynamical Mean-Field Theory of Strongly Correlated Fermion Systems and the Limit of Infinite Dimensions*, *Rev. Mod. Phys.* **68**, 13 (1996).
- [29] G. Kotliar, S. Y. Savrasov, K. Haule, V. S. Oudovenko, O. Parcollet, and C. A. Marianetti, *Electronic Structure Calculations with Dynamical Mean-Field Theory*, *Rev. Mod. Phys.* **78**, 865 (2006).
- [30] P. Blaha, K. Schwarz, G. Madsen, D. Kvasnicka, and J. Luitz, *wien2k, An Augmented Plane Wave+Local Orbitals Program for Calculating Crystal Properties* (Karlheinz Schwarz, Technische Universität Wien, Austria, 2001), ISBN: 3-9501031-1-2.

- [31] J. Kuneš, R. Arita, P. Wissgott, A. Toschi, H. Ikeda, and K. Held, *Wien2wannier: From Linearized Augmented Plane Waves to Maximally Localized Wannier Functions*, *Comput. Phys. Commun.* **181**, 1888 (2010).
- [32] A. A. Mostofi, J. R. Yates, G. Pizzi, Y.-S. Lee, I. Souza, D. Vanderbilt, and N. Marzari, *An Updated Version of wannier90: A Tool for Obtaining Maximally-Localised Wannier Functions*, *Comput. Phys. Commun.* **185**, 2309 (2014).
- [33] A. G. Petukhov, I. I. Mazin, L. Chioncel, and A. I. Lichtenstein, *Correlated Metals and the LDA + U Method*, *Phys. Rev. B* **67**, 153106 (2003).
- [34] E. Gorelov, M. Karolak, T. O. Wehling, F. Lechermann, A. I. Lichtenstein, and E. Pavarini, *Nature of the Mott Transition in Ca₂RuO₄*, *Phys. Rev. Lett.* **104**, 226401 (2010).
- [35] Z. V. Pchelkina, I. A. Nekrasov, T. Pruschke, A. Sekiyama, S. Suga, V. I. Anisimov, and D. Vollhardt, *Evidence for Strong Electronic Correlations in the Spectra of Sr₂RuO₄*, *Phys. Rev. B* **75**, 035122 (2007).
- [36] P. Werner, A. Comanac, L. de' Medici, M. Troyer, and A. J. Millis, *Continuous-Time Solver for Quantum Impurity Models*, *Phys. Rev. Lett.* **97**, 076405 (2006).
- [37] L. Boehnke, H. Hafermann, M. Ferrero, F. Lechermann, and O. Parcollet, *Orthogonal Polynomial Representation of Imaginary-Time Green's Functions*, *Phys. Rev. B* **84**, 075145 (2011).
- [38] H. Hafermann, K. R. Patton, and P. Werner, *Improved Estimators for the Self-Energy and Vertex Function in Hybridization-Expansion Continuous-Time Quantum Monte Carlo Simulations*, *Phys. Rev. B* **85**, 205106 (2012).
- [39] M. Karolak, G. Ulm, T. Wehling, V. Mazurenko, A. Poteryaev, and A. Lichtenstein, *Double Counting in {LDA} + DMFT—The Example of NiO*, *J. Electron Spectrosc. Relat. Phenom.* **181**, 11 (2010).
- [40] X. Wang, E. Gull, L. de' Medici, M. Capone, and A. J. Millis, *Antiferromagnetism and the Gap of a Mott Insulator: Results from Analytic Continuation of the Self-Energy*, *Phys. Rev. B* **80**, 045101 (2009).
- [41] M. Jarrell and J. E. Gubernatis, *Bayesian Inference and the Analytic Continuation of Imaginary-Time Quantum Monte Carlo Data*, *Phys. Rep.* **269**, 133 (1996).
- [42] A. Hariki, T. Uozumi, and J. Kuneš, *LDA + DMFT Approach to Core-Level Spectroscopy: Application to 3d Transition Metal Compounds*, *Phys. Rev. B* **96**, 045111 (2017).
- [43] A. Hariki, M. Winder, T. Uozumi, and J. Kuneš, *LDA + DMFT Approach to Resonant Inelastic X-Ray Scattering in Correlated Materials*, *Phys. Rev. B* **101**, 115130 (2020).
- [44] M. Ghiasi, A. Hariki, M. Winder, J. Kuneš, A. Regoutz, T.-L. Lee, Y. Hu, J.-P. Rueff, and F. M. F. de Groot, *Charge-Transfer Effect in Hard X-Ray 1s and 2p Photoemission Spectra: LDA + DMFT and Cluster-Model Analysis*, *Phys. Rev. B* **100**, 075146 (2019).
- [45] L. H. Tjeng, C. T. Chen, J. Ghijsen, P. Rudolf, and F. Sette, *Giant Cu 2p Resonances in CuO Valence-Band Photoemission*, *Phys. Rev. Lett.* **67**, 501 (1991).
- [46] L. H. Tjeng, C. T. Chen, and S.-W. Cheong, *Comparative Soft-X-Ray Resonant-Photoemission Study on Bi₂Sr₂CaCu₂O₈, CuO, and Cu₂O*, *Phys. Rev. B* **45**, 8205 (1992).
- [47] H. Eskes, L. H. Tjeng, and G. A. Sawatzky, *Cluster-Model Calculation of the Electronic Structure of CuO: A Model Material for the High-T_c Superconductors*, *Phys. Rev. B* **41**, 288 (1990).
- [48] Y.-Y. Chin, Z. Hu, Y. Shimakawa, J. Yang, Y. Long, A. Tanaka, L. H. Tjeng, H.-J. Lin, and C.-T. Chen, *Charge and Spin Degrees of Freedom in A-Site Ordered YCu₃Co₄O₁₂ and CaCu₃Co₄O₁₂*, *Phys. Rev. B* **103**, 115149 (2021).
- [49] T. Böske, K. Maiti, O. Knauff, K. Ruck, M. S. Golden, G. Krabbes, J. Fink, T. Osafune, N. Motoyama, H. Eisaki, and S. Uchida, *Cu-O Network-Dependent Core-Hole Screening in Low-Dimensional Cuprate Systems: A High-Resolution X-Ray Photoemission Study*, *Phys. Rev. B* **57**, 138 (1998).
- [50] T. T. Tran, K. Takubo, T. Mizokawa, W. Kobayashi, and I. Terasaki, *Electronic Structure of CaCu₃Ru₄O₁₂ studied by X-Ray Photoemission Spectroscopy*, *Phys. Rev. B* **73**, 193105 (2006).
- [51] J. Ghijsen, L. H. Tjeng, J. van Elp, H. Eskes, J. Westerink, G. A. Sawatzky, and M. T. Czyzyk, *Electronic Structure of Cu₂O and CuO*, *Phys. Rev. B* **38**, 11322 (1988).
- [52] A. Tanaka and T. Jo, *Resonant 3d, 3p and 3s Photoemission in Transition Metal Oxides Predicted at 2p Threshold*, *J. Phys. Soc. Jpn.* **63**, 2788 (1994).
- [53] The parameters for the CuO₄ calculations are tuned based on the values taken from Ref. [47]: $U_{dd} = 7.8$, $U_{pd} = 9.0$, $\Delta = 4.0$, $pd\sigma = -1.44$, $pd\pi = 0.625$, and $T_{pp} = 1.3$. Additionally, we set the ionic crystal field parameters to $10Dq = 1.0$, $Ds = 0.025$, and $Dt = 0.05$. All values are in eV.
- [54] M. Taguchi *et al.*, *Evidence for Suppressed Screening on the Surface of High Temperature La_{2-x}Sr_xCuO₄ and Nd_{2-x}Ce_xCuO₄ Superconductors*, *Phys. Rev. Lett.* **95**, 177002 (2005).
- [55] G. Panaccione, F. Offi, P. Torelli, G. Vanko, O. Tjernberg, P. Lacovig, A. Guarino, A. Fondacaro, A. Nigro, M. Sacchi, N. B. Brookes, and G. Monaco, *Analysis of Surface-Bulk Screening Competition in the Electron-Doped Nd_{2-x}Ce_xCuO₄ Cuprate Using X-Ray Photoemission Spectroscopy*, *Phys. Rev. B* **77**, 125133 (2008).
- [56] M. B. Trzhaskovskaya, V. I. Nefedov, and V. G. Yarzhevsky, *Photoelectron Angular Distribution Parameters for Elements $z = 1$ to $z = 54$ in the Photoelectron Energy Range 1005000 eV*, *At. Data Nucl. Data Tables* **77**, 97 (2001).
- [57] M. B. Trzhaskovskaya, V. K. Nikulin, V. I. Nefedov, and V. G. Yarzhevsky, *Non-dipole Second Order Parameters of the Photoelectron Angular Distribution for Elements $z = 1-100$ in the Photoelectron Energy Range 110 keV*, *At. Data Nucl. Data Tables* **92**, 245 (2006).
- [58] J. J. Yeh and I. Lindau, *Atomic Subshell Photoionization Cross Sections and Asymmetry Parameters: $1 \leq z \leq 103$* , *At. Data Nucl. Data Tables* **32**, 1 (1985).
- [59] In order to reach lower temperatures, we use a model without the empty Ru 4d e_g states here. The equivalence of Cu 3d xy spectra in the models with and without Ru 4d e_g states is established in Appendix D.
- [60] S. Burdin, A. Georges, and D. R. Grempel, *Coherence Scale of the Kondo Lattice*, *Phys. Rev. Lett.* **85**, 1048 (2000).

- [61] T. Pruschke, R. Bulla, and M. Jarrell, *Low-Energy Scale of the Periodic Anderson Model*, *Phys. Rev. B* **61**, 12799 (2000).
- [62] A. Hariki, A. Yamanaka, and T. Uozumi, *Theory of Spin-State Selective Nonlocal Screening in Co 2p X-Ray Photoemission Spectrum of LaCoO₃*, *J. Phys. Soc. Jpn.* **84**, 073706 (2015).
- [63] V. Křápek, P. Novák, J. Kuneš, D. Novoselov, D. M. Korotin, and V. I. Anisimov, *Spin State Transition and Covalent Bonding in LaCoO₃*, *Phys. Rev. B* **86**, 195104 (2012).
- [64] A. Hariki, A. Hausoel, G. Sangiovanni, and J. Kuneš, *DFT + DMFT Study on Soft Moment Magnetism and Covalent Bonding in SrRu₂O₆*, *Phys. Rev. B* **96**, 155135 (2017).
- [65] E. R. Ylvisaker, J. Kuneš, A. K. McMahan, and W. E. Pickett, *Charge Fluctuations and the Valence Transition in Yb under Pressure*, *Phys. Rev. Lett.* **102**, 246401 (2009).
- [66] G. Cao, O. Korneta, S. Chikara, L. E. DeLong, and P. Schlottmann, *Non-Fermi-Liquid Behavior in Single-Crystal CaRuO₃: Comparison to Ferromagnetic SrRuO₃*, *Solid State Commun.* **148**, 305 (2008).
- [67] N. Kikugawa, L. Balicas, and A. P. Mackenzie, *Physical Properties of Single-Crystalline CaRuO₃ Grown by a Floating-Zone Method*, *J. Phys. Soc. Jpn.* **78**, 014701 (2009).
- [68] Y. Liu, H. P. Nair, J. P. Ruf, D. G. Schlom, and K. M. Shen, *Revealing the Hidden Heavy Fermi Liquid in CaRuO₃*, *Phys. Rev. B* **98**, 041110(R) (2018).